Temperature-dependent mechanical properties of $Ti_{n+1}C_nO_2$ (n = 1, 2) MXene monolayers: a first-principles study

Rasoul Khaledialidusti,[*1] Babak Anasori,[*2] Afrooz Barnoush[1]

[1]Department of Mechanical and Industrial Engineering, Norwegian University of Science and Technology (NTNU), 7491 Trondheim, Norway.
[2] Department of Mechanical and Energy Engineering, and Integrated Nanosystems Development Institute, Purdue School of Engineering and Technology, Indiana University – Purdue University Indianapolis, Indianapolis, IN 46202, USA.

ABSTRACT

Two-dimensional (2D) transition metal carbides, corbonitrides, and nitrides (named as MXenes) have become of the fastest growing family of 2D materials in terms of compositions and their applications in different areas. One of the least explored properties of MXenes is their mechanical properties. While the basic elastic properties of MXenes have been studied by first-principles, the effects of temperature on the elastic properties have never been explored. In this study, we investigate temperature-dependent structural and mechanical properties of the titanium-containing MXenes ($Ti_{n+1}C_nO_2$ (n = 1, 2)) based on the first-principles calculations combined with quasi-harmonic approximation. The effective Young's modulus of a single layer of Ti_2CO_2 and $Ti_3C_2O_2$ is calculated to be 565 and 482 GPa, respectively, at 0 K. By increasing temperature to 1000 K, Young's moduli of Ti_2CO_2 and $Ti_3C_2O_2$ decrease to 469 GPa and 442 GPa, respectively, which indicates a larger reduction in stiffness in thinner MXenes at higher temperatures. Our calculations of the temperature-dependent bond strengths within MXenes showed that titanium and carbon atoms in $Ti_3C_2O_2$ form stronger bonds than Ti_2CO_2 and atomic bonds in Ti_2CO_2 lose their stiffness more than $Ti_3C_2O_2$ with increasing temperatures. The Debye temperature of these monolayers is also calculated to provide a comparison of the thermal conductivity between these monolayers, in which the results show that the $Ti_3C_2O_2$ has a higher thermal conductivity than Ti_2CO_2. Our calculated electronic properties results of the monolayers are also shown that the electrical conductivity of the monolayers would not change with temperature. Our study extends MXenes applications to high-temperature applications, such as structural composite components and aerospace coatings.

INTRODUCTION

Two-dimensional (2D) materials have attracted much attention and are widely studied due to their diverse applications in the fifteen years. Although graphene is the most recognized 2D material[1], other examples of 2D materials are transition metal dichalcogenides (*e.g.*, $NbSe_2$ and

This is the author's manuscript of the article published in final edited form as:

Khaledialidusti, R., Anasori, B., & Barnoush, A. (2020). Temperature-dependent mechanical properties of Tin+1CnO2 (n = 1, 2) MXene monolayers: A first-principles study. Physical Chemistry Chemical Physics, 22(6), 3414–3424. https://doi.org/10.1039/C9CP06721C

MoS_2)[2], *hexagonal* boron nitrides (*h*-BN)[3], and black phosphorous[4]. A large family of 2D transition metal carbides, carbonitrides, and nitrides (MXene) have been introduced in 2011 with the general formula of $M_{n+1}X_nT_x$ (n = 1, 2, and 3)[5,6], where M is an early transition metal, X stands for carbon and/or nitrogen, and T_x represents the surface termination (–O, –OH, and –F).

$Ti_3C_2T_x$ was the first MXene synthesized in 2011[5]. To date, about thirty different MXene compositions have been synthesized, while a large number have been predicted theoretically[7,8]. Among all the experimentally synthesized and theoretically predicted MXenes, titanium carbide MXenes are still the most extensively applied and studied[8]. The effects of different surface terminations on the stabilization, mechanical properties, and electronic properties of $Ti_3C_2T_x$ are studied using DFT[5,7,9,10]. It was predicted that the oxygen functional groups provide the most thermodynamic stabilization as compared to other surface terminations.

MXenes have unique combinations of properties and have been explored in different areas such as electromagnetic interference (EMI) shielding[11], wireless communication[12], membranes[13], Li-ion batteries[14,15], purifiers[16], catalysts[17], electronics[18–20], optical[21], thermoelectric[22,23], sensing devices[24,25], and photocatalytic reactions[26,27]. One of the least explored areas in the MXenes field is MXenes mechanical properties and their structural applications.

MXenes are predicted to have high Young's modulus in the range of 400-1000 GPa, depending on the composition, surface terminations, and the number of layers[7,9,28–34], and all are predicted to be stronger than their MAX phases[33]. It is found that surface terminations could make MXenes more mechanically flexible than their pristine MXenes. Additionally, the strength of MXenes functionalized by O is higher than those of terminated by F or OH[31,35]. It is shown that oxygen functional groups make a stronger bonding with the outer transition metal layers, because oxygen atoms gain more charges from transition metal atoms, compare to other types of surface terminations[9,30,31,35]. It is also reported that the strength of MXenes decreases by

increasing the thickness of MXene monolayer (increasing n) [28,31]. Graphene is known as the strongest 2D material with Young's modulus of almost 1 TPa for a graphene sheet made by mechanical exfoliation[36]. However, mechanical exfoliation can only produce small amounts of pure graphene and large-scale production is very difficult if not impossible[37]. One method that can be easily scaled up is solution-processing. By solution-processing of graphene, graphene oxide is produced, which has a significantly lower Young's modulus of 200 GPa[38]. MXenes are a family of 2D materials than can be solution-processed. The measured Young's modulus for a solution-processed $Ti_3C_2T_x$ was determined at room temperature to be 330 ± 30 GPa[29]. This high value of Young's modulus makes $Ti_3C_2T_x$ MXene the stronger solution-processed 2D material[29].

Although much attention has been devoted to the mechanical properties of bare and functionalized MXenes using DFT calculations at 0 K, temperature-dependent mechanical properties of MXenes have not been studied. Therefore, it is not possible to compare the DFT calculations and the experimental results unless the experimental results are measured at 0 K and are corrected for zero-point vibration effects, which are not present in standard DFT calculations[39,40]. Understanding the behavior of MXenes at different temperatures is required to pave way for their applications including surrounding high-temperatures such as structural composite applications[41].

In this paper, we study the temperature-dependent structural and mechanical properties (elastic constants, Young's modulus, Poisson's ratio, and in-plane stiffness) of Ti_2CO_2 and $Ti_3C_2O_2$ MXenes using density functional theory combined with quasi-harmonic approximation (DFT-QHA)[39,42] method by considering zero-point energy. We also provide details of comparisons with previous theoretical results and some experimental results for graphene, and for both bare and functionalized $Ti_{n+1}C_nO_2$ (n = 1, 2). Our findings provide information on how the structural

and mechanical properties of the corresponding MXenes change with temperature, which is useful for MXenes high-temperature applications.

I. THEORETICAL METHODS

DFT calculations in conjunction with projector augmented wave (PAW) potentials are performed using the Vienna *Ab-initio* Simulation Package (VASP)[43–46]. The generalized gradient approximation (GGA) using the functional of Perdew, Bruke and Ernzerhof (PBE)[47,48] are chosen as the exchange-correlation functional. A Conjugate gradient scheme is applied with an iterative relaxation of the atomic positions with the residual forces acting on each atom of 0.01 eV/Å and a total energy convergence of 10^{-6} eV/cell. The cut-off energy of 550 eV is set for all the calculations. For the crystal optimization of a 1 × 1 × 1 unit cell of 2D $Ti_{n+1}C_nO_2$ (n = 1, 2) MXenes, a 16 × 16 × 1 Monkhorst−Pack[49] k-point mesh for the Brillouin zone sampling is used. Different cut-off energies and k-point meshes are tested until the energy convergence criterion of 1 meV is achieved with these computational parameters. The Methfessel–Paxton smearing scheme with a smearing width of 0.1 eV is used for the determination of partial occupancies.

The monolayer of $Ti_{n+1}C_nO_2$ (n = 1, 2) MXenes consists of single (n = 1) or double (n = 2) hexagonal layers of C atoms which are sandwiched between n + 1 monoatomic hexagonal Ti planes (**Fig. 1**). We build the MXene monolayers with the functional groups associated with the most energetically stable configuration predicted[9,10,20], as shown in **Fig. 1**. For performing DFT calculations, monolayers are placed at the base of the simulation cell and a large vacuum region of 20 Å is added above the upper layer along the z-direction to avoid interactions between a single MXene sheet and the periodically repeated images.

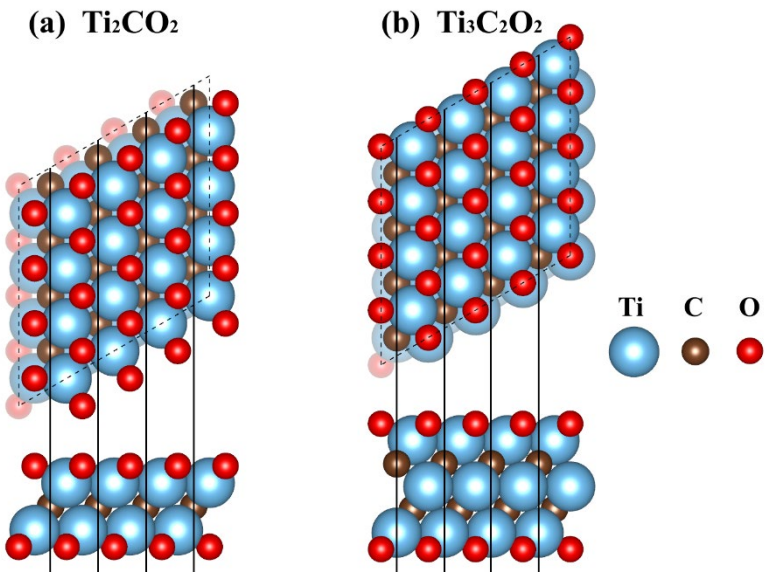

Figure 1. Top-view (top) and side-view (bottom) of 4×4×1 supercell of (a) Ti_2CO_2 and (b) $Ti_3C_2O_2$ structures.

After structural optimization, thermal properties and temperature-dependent mechanical properties of MXenes are studied by first-principles through phonon calculations performed by density functional perturbation theory (DFPT)[50,51]. The phonon dispersions are calculated by using the PHONOPY code[40,42] within a 4 × 4 × 1 supercell of the MXene monolayers to guarantee the convergence of phonon dispersion. The k-points of 4 × 4 × 1 generated with the Monkhorst−Pack[49] scheme are applied and the cut-off energy of 550 eV is set. To ensure adequate precision of the generated force constants, the criterion for energy convergence is set to 10^{-8} eV/cell. Since considering the long-range dispersion forces are necessary for the precise description of the atomic interactions of MXenes during tensile deformation, we employed the correction according to the Grimme method[52] for the van der Waals interaction (DFT-D2). However, the Coulomb effect (U) for the localized 3d electrons of Ti atoms is ignored since it has been tested and a negligible effect on the results has been noticed.

We employed the quasi-anharmonic approximation (QHA)[40], in which the anharmonicity volume dependence of phonon properties are applied. The temperature-dependent properties of MXenes are calculated by combining DFT with QHA (DFT-QHA)[39,42]. By knowing the phonon frequencies, the energy level of the system and Gibbs energy can be determined, and

further thermodynamic properties can be calculated. The pressure value is zero and the Gibbs energy is equal to the Helmholtz free energy. The Helmholtz free energy F at given temperature and volume are computed using $F(T, V) = E_{DFT}(V) + F_{vib}(T, V)$, where $E_{DFT}(V)$ is the DFT total energy and $F_{vib}(T, V)$ is the vibrational free energy[39,40,42].

In the following, we briefly describe the method employed for calculating temperature-dependent lattice parameters and mechanical properties of 2D $Ti_{n+1}C_nO_2$ (n = 1, 2) MXenes from phonon density of states by using the QHA. More details of the calculation for 3D and 2D crystals are found in Refs.[53,54] and Ref.[55], respectively.

A. Temperature-dependent structural optimization

The Helmholtz energy is a function of all lattice parameters in a crystal. Then, the non-equilibrium Helmholtz energy should be minimized based on the multiple variable functions (*i.e.*, lattice parameters) to find the Helmholtz energy at equilibrium state, which is currently not possible by using the first-principles method. Hence, in order to avoid the full minimization of non-equilibrium Helmholtz energy, we derived the Helmholtz energy functions with one deformation strain ε, which is defined as $\varepsilon = {}^{a}/_{a_0}$ (a and a_0 are the equilibrium and strained lattice parameters). Therefore, the non-equilibrium Helmholtz energy can be calculated as:

$$F[X(\varepsilon);T] = E[X(\varepsilon)] + F_{vib}[X(\varepsilon);T], \qquad (1)$$

where $E[X(\varepsilon)]$ is the total energy of the specific deforming configuration. $F_{vib}[X(\varepsilon); T]$ is the vibrational Helmholtz free energy calculated from phonon density states using the DFT-QHA. For a fixed deformation mode, the equilibrium Helmholtz energy, which is only a function of temperature T, can be obtained by determining the minimum point of the non-equilibrium Helmholtz energy curve with respect to the deformation strain ε at each temperature.

$$F^*[\varepsilon_T^0;T] = \min\{E[X(\varepsilon)] + F_{vib}[X(\varepsilon);T]\}, \qquad (2)$$

By solving Eq. (2), the equilibrium deformation strain ε_T^0 at given temperature T can be found, and, then the lattice parameters can be calculated. Since $Ti_{n+1}C_nO_2$ (n = 1, 2) MXenes has

hexagonal symmetry, we chose the biaxial deformation tensor with ε up to ± 3% and increments of 0.5% to obtain the equilibrium lattice parameter at each temperature from 0 to 1000 K and increments of 50 K. The ε_T^0 is obtained by polynomial fitting the non-equilibrium Helmholtz free energies at each temperature, as shown in Sec. II A. Then, the lattice parameter for hexagonal MXenes can be determined as:

$$a_T = (1 + \varepsilon_T^0)a_0, \quad (3)$$

where a_0 is the optimized lattice parameter at 0 K calculated from the DFT calculation and a_T is the equilibrium lattice parameter at temperature T.

B. Temperature-dependent elastic constants

After calculating the equilibrium lattice parameter at each temperature, we calculated the isothermal elastic constants, which can be deliberated as strain derivatives of the Helmholtz free energy using **Eq. 1**. Due to the basic symmetry of a hexagonal MXene sheet, the elastic constant matrix is contained only two independent elastic constants of c_{11} and c_{12}. To calculate these two constants, two sets of deformed crystals are required to be built that lead to two sets of the Helmholtz energy F[X(ε); T] curves with respect to strain ε at a given temperature. We chose one uniaxial deformation tensor (*i.e.*, (ε, 0, 0, 0) and one biaxial deformation tensor (*i.e.*, (ε, 0, ε, 0) as two deformation modes to execute the QHA calculations for the temperature-dependent elastic constants of c_{11}^T and c_{12}^T. Then, the two sets of the Helmholtz energy per unit cell area with respect to the strain ε are calculated with ε up to ± 3% and increments of 0.5% at different temperatures from 0 to 1000 K and increments of 50 K. For the two deformation modes, the curves of the Helmholtz energy per unit cell area with respect to the deformation strain ε are obtained by the polynomial fitting. Further, the second-order derivatives of these curves with respect to the deformation strain ε corresponds to the independent elastic constants or their linear combination. The isothermal elastic constants are calculated by solving the

following system of linear equations giving the correlation between these second-order strain derivatives and the linear combination of isothermal elastic constants.

$$\begin{Bmatrix} c_{11}^T = D_1^T \\ 2c_{11}^T + 2c_{12}^T = D_2^T \end{Bmatrix} \quad (4)$$

where D_1^T and D_2^T are the second-order strain derivatives of the Helmholtz free energy under the two deformation modes, and, c_{11}^T and c_{12}^T are the elastic constants at a given temperature and zero pressure. After calculating the clastic constants, Young's modulus (E) and Poisson's ratio (ν) are calculated for small deformation applied on a hexagonal MXene using:

$$E^T = \frac{(c_{11}^T)^2 - (c_{12}^T)^2}{c_{11}^T} \quad (5)$$

$$\nu^T = {c_{12}^T}\Big/{c_{11}^T} \quad (6)$$

Since applying the uniaxial stress can lead to non-uniform biaxial stress conditions, we performed the geometry relaxation for both the lattice basis vectors and the atomic coordinates to make sure that the MXenes are under uniaxial stress. In order to achieve this goal, the applied in-plane strain component is kept fixed and the other in-plane strain component is relaxed until their conjugate stress components reach less than 0.1 GP and the dimensional length normal to the monolayers (Z-direction) is fixed to provide enough thickness of vacuum space. It is worth noting that the Poisson's ratio could be also calculated based on the dimensional length changes in X and Y direction during uniaxial deformation applied in addition to the formula based on the c_{11} and c_{22} constants in Eq. (6).

C. Temperature-dependent in-plane stiffness constant

The in-plane stiffness (C) is a more representative parameter for the strength than Young's modulus for 2D materials since the thickness of a monolayer structure is uncertain. The in-plane stiffness (C) has extensively been used for 2D materials at 0 K[31,32,56]. We calculated this parameter for the MXene monolayers by fitting the initial slope of the stress-strain curve under

biaxial tension at different temperatures. In order to achieve the stress-strain curves, first, it is required to obtain the equilibrium lattice configuration at each temperature and, then, stretch the crystal with the constant growth of $\Delta\varepsilon = 0.005$. Second, the crystal is relaxed while the lattice parameters are fixed to confirm that the other dominant stress perpendicular to the direction of tension is zero. After obtaining the configuration lattice $X(\varepsilon)^T$ at given temperature T, the Helmholtz energy for that configuration is calculated using **Eq. 1**. Finally, the stress-strain curves are obtained by:

$$\sigma(\varepsilon, T) = \frac{1+\varepsilon}{V(\varepsilon)^T}\frac{dF(\varepsilon,T)}{d\varepsilon}, \qquad (7)$$

where $\sigma(\varepsilon, T)$ and $V(\varepsilon)^T$ are the stress and volume of the structure under the strain of ε, and $F(\varepsilon, T)$ is the Helmholtz energy of the deformed crystal. Since forces are averaged over the entire system including the vacuum space in DFT calculations, the stress is scaled by H/d_0, where H is the cell length along the z-direction and d_0 is the effective thickness of the MXene monolayers, in order to avoid the effect of the vacuum region.

II. RESULTS AND DISCUSSION

In order to study temperature-dependent mechanical properties of 2D $Ti_{n+1}C_nO_2$ (n = 1, 2) MXenes, first, we focus on the geometry optimization at different temperatures in order to have an understanding of the structural and atomic spacing behavior of MXenes with temperature. Then, we present results for temperature-dependent mechanical properties of MXenes such as elastic constants, Poisson's ratio, Young's modulus, and in-plane stiffness. The results are compared with the previously published studies on $Ti_{n+1}C_nO_2$ (n = 1, 2) MXenes, Bulk TiC, pristine Ti_2C, and pristine Ti_3C_2 at 0 K.

A. Temperature-dependent structural optimization

Fig. 2a shows the calculated ***a*** lattice parameter (a-LPs) of Ti_2CO_2 and $Ti_3C_2O_2$ MXenes with respect to temperature. For calculating the a-LPs of MXenes, we first calculated their Helmholtz energy with respect to thirteen different volumes under biaxial deformation tensor

at different temperatures, as shown in **Figs. 2b-2c**. The calculated Helmholtz energies are represented by the filled blue circles in **Figs. 2b-2c**. The twenty curves are obtained by fitting to the equation of states (EOS) at temperatures from 0 to 950 K with 50 K steps. The minimum values of each curve are illustrated by the cross red symbols in **Figs. 2b-2c** which are the equilibrium Helmholtz energies at the temperatures and the respective equilibrium volumes are simultaneously found.

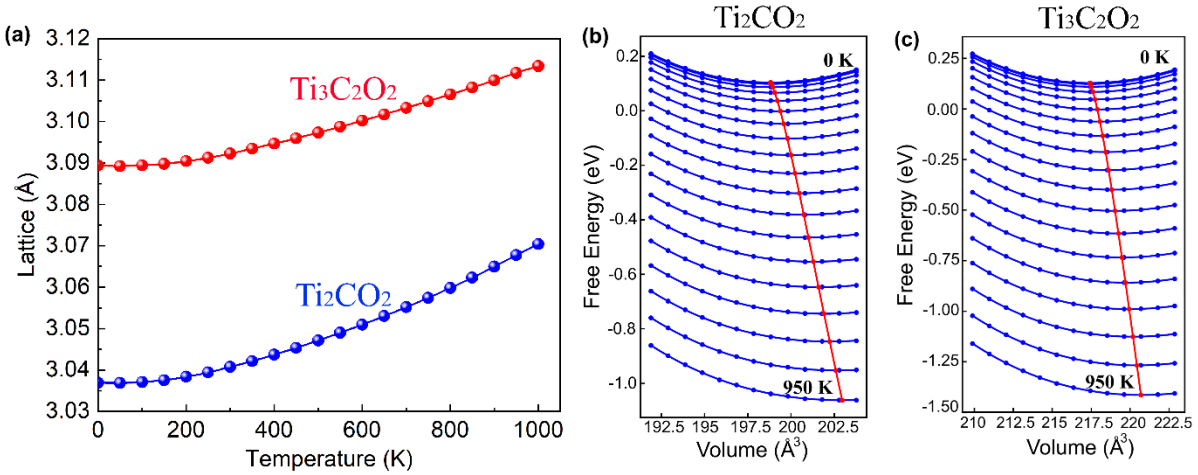

Figure 2. (a) Temperature-dependent *a* lattice parameters of Ti_2CO_2 and $Ti_3C_2O_2$ MXenes. Helmholtz energy of (b) Ti_2CO_2 and (c) $Ti_3C_2O_2$ MXenes as a function of volume at a temperature from 0 K to 950 K with 50 K steps are illustrated by filled blue circles, which are fit by the solid blue curves. The minimum energy of the curves is shown by the red symbols which determine the equilibrium volumes at each temperature. The red solid lines passing through the equilibrium volumes are guides to the eye.

The MXenes' *a*-LPs are plotted by using obtained equilibrium volumes at each temperature, as shown in **Fig. 2a**. In the present study, the *a*-LPs of 3.037 Å and 3.089 Å are calculated for Ti_2CO_2 and $Ti_3C_2O_2$ MXenes at 0 K, respectively. The presently calculated lattice constants are close to previously calculated values of 3.032[31] Å and 3.035[20] Å for Ti_2CO_2 and 3.10[57] Å for $Ti_3C_2O_2$. The results show that the lattice parameter of MXenes does not considerably change at temperatures T < 100 K unlike single-layer graphene with a negative thermal expansion at temperatures T < 400 K[58]. By further increasing temperature, the *a*-LPs start expanding and at 1000 K their values become 3.070 Å (1.09 %) and 3.113 Å (0.78 %) for Ti_2CO_2 and $Ti_3C_2O_2$ MXenes, respectively. Based on these values, Ti_2CO_2 has slightly larger growth in interatomic distances than $Ti_3C_2O_2$ with increasing temperature. This could indicate

that surface functionalization has a greater effect on the bond strength in the thinner MXenes. It was found by valence X-ray photoelectron spectroscopy (XPS) spectra that the Ti-C bond strength of $Ti_{n+1}C_nT_x$ MXenes depends on the carbon content and atomic layer thickness, and it is weaker in Ti_2CT_x than that in $Ti_3C_2T_x$.[59] In our calculations, we assumed that oxygen terminations stay on MXenes' surfaces and no surface terminations dissociations occur because of increase in the temperature above ~ 550 ºC. It was observed recently that heating Ti-containing MXenes in an inert environment leads to dissociation of MXene flakes terminations[60].

In order to better understanding of temperature dependence of bond strengths, we employed the crystal orbital Hamilton population (COHP) analysis[61] to calculate the bond strengths of the MXenes. The COHP analysis indicates bonding, nonbonding, and antibonding contributions to the band-structure energy using localized atomic basis sets and the energy integration of the COHP calculations (ICOHP) for a pair of atoms up to the Fermi energy provides the bond strength.[62] It is worth noting that the strength of the covalency and not the iconicity of a bond is considered by the ICOHP, which is characterized by the number of electrons of a specific atom shared with other atoms when forming chemical bonds. More details of ICOHP calculations can be found in the works of Khazaei et al.[63,64].

Fig. 3 shows the results of temperature-dependent ICOHP and atom-atom distance calculations for Ti–O, Ti–C, Ti–Ti, and C–C bonds in Ti_2CO_2 and $Ti_3C_2O_2$ MXenes. The results of ICOHP indicate that the bond strengths between titanium and carbon atoms in $Ti_3C_2O_2$ are stiffer than those in Ti_2CO_2 while oxygen atoms form stronger bonds with outer titanium atoms in Ti_2CO_2 than $Ti_3C_2O_2$. This indicates that more charge is transferred from the Ti atoms to oxygen surface atoms in thinner Ti_2CO_2 than thicker $Ti_3C_2O_2$. Generally, the bond strengths become weaker at higher temperatures as the atom-atom distances increase; however, our results show that the C–C bond in $Ti_3C_2O_2$ decreases slightly by increasing the temperature, which leads to

higher ICOHP energy (possibly stiffer C-C bonds) (**Figs. 3g** and **3h**). The weakening of the bond strengths is more significant in Ti_2CO_2 than $Ti_3C_2O_2$, especially for Ti–Ti bond. Since the bonds between various atoms within Ti_2CO_2 lose their stiffness more than $Ti_3C_2O_2$ at higher temperatures, we would expect a larger effect on the mechanical properties for Ti_2CO_2 rather than $Ti_3C_2O_2$ at those temperatures.

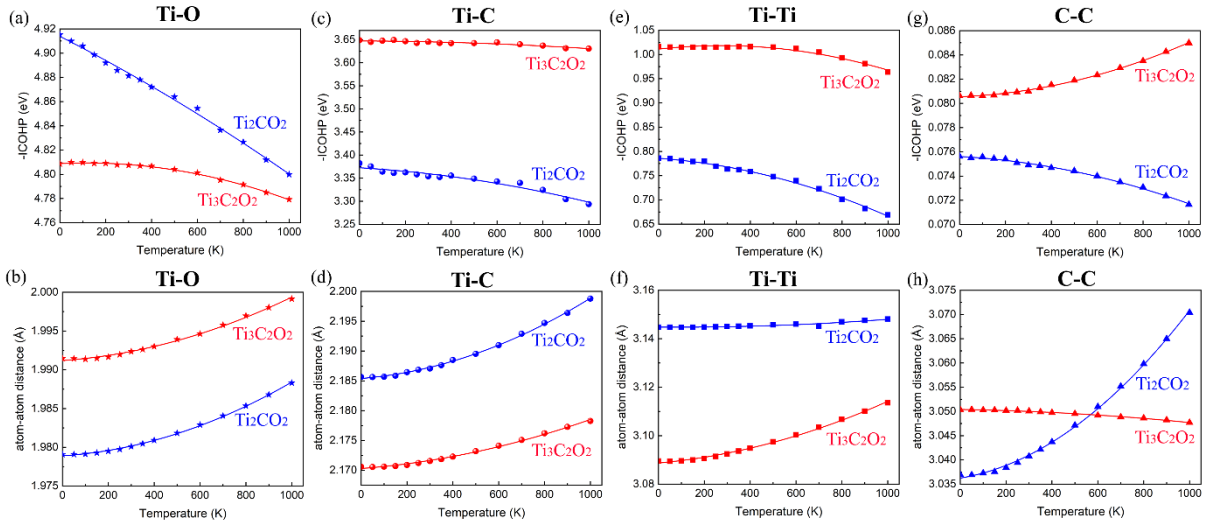

Figure 3. Temperature-dependent integrated crystal orbital Hamilton population (ICOHP) and atom-atom distance between various atoms in the MXenes. (a)-(b) Ti-O, (c)-(d) Ti-C, (e)-(f) Ti-Ti, and (g)-(h) C-C bonds. The solid lines indicate the polynomial fit to the results.

B. Temperature-dependent elastic constants

We calculated temperature-dependent elastic constants and Poisson's ratio using the methodology explained in Sec. II. Then, Young's modulus is calculated from the elastic constants using **Eq. 5**. In previous DFT studies[31,32], Young's modulus was calculated directly by a linear fit to the stress-strain curve and, hence, no elastic constants were reported.

Fig. 4a shows the results of temperature-dependent elastic constants (c_{11} and c_{12}) of Ti_2CO_2 and $Ti_3C_2O_2$. Generally, the elastic constants for MXenes decrease with increasing temperature. This decrease is more significant for Ti_2CO_2 so that its c_{12} becomes less than that of $Ti_3C_2O_2$ at temperatures higher than 600 K. The larger change of elastic constants in Ti_2CT_x might be due to temperature effect on the bond strengths within thinner MXenes that the bonds between

different atoms lose their stiffness more significantly at higher temperatures in Ti_2CO_2 than $Ti_3C_2O_2$ (see **Fig. 3**).

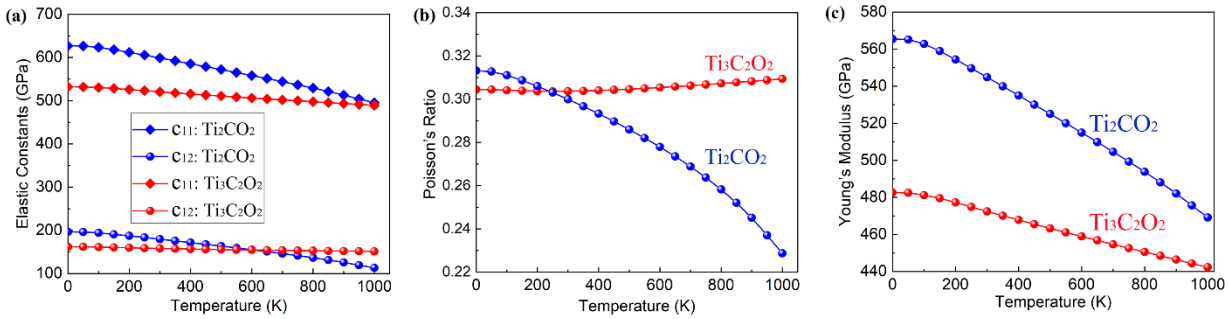

Figure 4. Temperature-dependent (a) elastic constants (c_{11} and c_{12}), (b) Poisson's ratio, and (c) Young's modulus of Ti_2CO_2 and $Ti_3C_2O_2$ MXenes.

In order to have a more precise comparison, the calculated elastic constants, Poisson's ratio, and Young's modulus of MXenes at three different temperatures of 0 K, 300 K, 1000 K are listed in **Table 1**; furthermore, the previously calculated elastic constants of graphene by DFT-QHA with considering zero-point energy at the corresponding temperatures taken from Ref.[55] are also presented. The results show that c_{11} of Ti_2CO_2 decreases by almost 4.5% and 21% at 300 K and 1000 K, respectively, while the changes in its c_{12} are almost doubled to 8.5% and 42.3% at the similar temperatures. The elastic constants of $Ti_3C_2O_2$ are less varied than Ti_2CO_2, and $Ti_3C_2O_2$ c_{11} decreases by almost 2.1% and 8.0% at 300 K and 1000 K, respectively, while c_{12} decreases by almost 2.4% and 6.5% at the corresponding temperatures. In comparison to graphene with E of 1173 GPa[38], it is found that $Ti_{n+1}C_nO_2$ MXenes are less stiff, particularly $Ti_3C_2O_2$. Additionally, MXenes' stiffness values decrease more than that of graphene at higher temperatures, especially for Ti_2CO_2. However, as it was described before and in previous studies[28,29] comparing $Ti_{n+1}C_nT_x$ to graphene oxide as a solution-processed material is more accurate because of graphene oxide and MXenes have surface functionalization. It was found that the stiffness of graphene (at ~1100 GPa) reduces drastically to ~ 210 GPa, which is less than that of $Ti_{n+1}C_nT_x$ by oxygen functionalization[29]. Therefore, the mechanical properties of

one-atom-thick monolayer graphene could be affected stronger by surface functionalization than the few-atom-thick $Ti_{n+1}C_nO_2$ flakes.

Table 1. Elastic constants, Poisson's ratio (ν), and Young's modulus (E) for $Ti_{n+1}C_nO_2$ (n = 1, 2) MXenes at 0 K, 300 K, and 1000 K. For comparison, the DFT-QHA calculated elastic constants and Young's modulus for graphene as given in Ref.[55] are also stated. The values are in GPa. The percentage of variation are listed in parentheses

	Temperature (K)	c_{11} (GPa)	c_{12} (GPa)	ν	E (GPa)
Ti_2CO_2	0	627.03	196.49	0.312	565
	300	598.79 (4.5%)	179.72 (8.5%)	0.300 (3.8%)	545 (3.5%)
	1000	495.16 (21.0%)	113.34 (42.3%)	0.229 (26.6)	469 (17.0%)
$Ti_3C_2O_2$	0	531.96	162.04	0.304	482
	300	520.54 (2.1%)	158.17 (2.4%)	0.304 (0.0%)	472 (2.1%)
	1000	489.23 (8.0%)	151.44 (6.5%)	0.309 (1.6%)	442 (8.3%)
graphene	0	1208.78	208.81	0.173	1173
	300	1205.76 (0.25%)	205.56 (1.6%)	0.171 (1.16%)	1171 (0.2%)
	1000	1178.46 (2.5%)	192.76 (7.7%)	0.164 (5.2%)	1147 (2.2%)

The calculated Poisson's ratio and Young's modulus of MXenes at different temperatures are shown in **Figs. 4b** and **4c**. The calculated results at 0 K in addition to the available DFT results for the MXenes are given in **Table 2** as well as Young's modulus of graphene calculated by DFT-QHA by considering zero-point energy at the corresponding temperatures taken from Ref.[55].

We calculated E = 565 GPa at 0 K for Ti_2CO_2 MXene, which is very close to E = 567 GPa of Ref.[31] and E = 570 GPa of Ref.[32] calculated by a linear fit to the stress-strain curve under uniaxial tensile strains using *ab initio* method. The calculated Young's modulus of 482 GPa for $Ti_3C_2O_2$ MXene at 0 K in our study is also very close the value of 484 GPa calculated by DFT of Ref.[31], while our calculated Young's modulus varies from the value of 369 GPa derived by DFT of Ref.[30] due to difference in the layer thickness applied. For $Ti_3C_2T_x$, our calculated Young's modulus value is 482 GPa, which is higher than the 333 ± 30 GPa[29] effective Young's modulus determined experimentally for $Ti_3C_2T_x$ MXene at room temperature. At 472 GPa, our calculated Young's modulus value at room temperature is still significantly higher than the experimentally measured one. The main reason for the lower value for the measured Young's modulus (333 ± 30 GPa) is the presence of defects and also the mixture of surface functionality

(–O, –OH, and –F) in the solution-processed $Ti_3C_2T_x$ MXene[30,35]. It was found that oxygen functionalized MXenes causes a larger elastic constant c_{11} comparing to those functionalized with –F or –OH because of more significant charge transfer from the inner Ti–C bonds to the outer surface ones by oxygen atoms[30,35]. In the present study, the value of 482 GPa is calculated for a Ti_3C_2 monolayer functionalized only by oxygen and without any defects.

Comparing the calculated values of Young's modulus for Ti_2C and Ti_3C_2 and the values calculated for Ti_2CO_2 (565 GPa) and $Ti_3C_2O_2$ (482 GPa) (see **Table 2**) in this study indicates that surface functionalization leads to decrease in Young's modulus of the MXenes. Additionally, these values show that thinner MXenes are mechanically stiffer than the thicker MXenes with similar compositions.

Our results of temperature-dependent Poisson's ratios of MXenes in **Fig. 4b** shows that the Poisson's ratios decrease slightly with temperature for Ti_2CO_2, while Poisson's ratio remains almost constant with increasing temperature for $Ti_3C_2O_2$ (**Fig. 4b**). This means that shear modulus decreases marginally with a smaller percentage than that of the moduli in tension and compression for Ti_2CO_2 at higher temperatures, while shear modulus and moduli in tension and compression decrease with almost the same rate for $Ti_3C_2O_2$ at higher temperatures. Our calculated results show that Young's modulus of Ti_2CO_2 decreases by 3.5% and 17.0% at 300 K and 1000 K, respectively, while it decreases less for $Ti_3C_2O_2$ by 2.1% and 8.3% at those temperatures (Fig. 4c). It is mainly because of the larger expansion in the interatomic distances and consequently more decrement in the bond strengths (**Fig. 3**) of Ti_2CO_2 than that of $Ti_3C_2O_2$ at higher temperatures, which might be resulted from the greater effect of the surface functionalization on the thinner MXenes.

Table 2. In-plane stiffness constant (C), Poisson's ratio (ν), and Young's modulus (E) of $Ti_{n+1}C_nO_2$ (n = 1, 2) MXene monolayers at 0 K. The in-plane stiffness constant, and Young's moduli are in GPa. The available first-principle results for the corresponding MXenes are included in parentes. For comparison, the previously calculated results for bulk TiC and 2D pristine $Ti_{n+1}C_n$ (n=1, 2) monolayers are also listed inside the parentheses.

	C	E (GPa)	ν
Ti_2CO_2	735, (745)[32]	565, (567)[31], (570)[32]	0.312, (0.303)[32]
$Ti_3C_2O_2$	616	482, (369)[30], (484)[31]	0.304
Bulk TiC	-	(524)[57], (450)[65,66]	(0.237)[57]
Pristine Ti_2C	(704)[32]	(588)[31], (577)[32], (513)[57]	(0.366)[32], (0.266)[57], (0.23)[34]
Pristine Ti_3C_2	-	(550)[31], (447)[57]	(0.241)[57]

C. Temperature-dependent in-plane stiffness constant

As stated in Sec II, because of the reduced dimensionality of 2D materials, it is more compatible to define the in-plane stiffness, *C*, rather than the classical 3D Young's modulus. We calculated this property for MXenes by fitting the initial slope of the stress-strain curves under biaxial tension at 0 K, 300 K, 600 K, and 900 K (Fig. 5).

We first compare our DFT-QHA results of the biaxial tensile stress-strain curve for Ti_2CO_2 and $Ti_3C_2O_2$ at 0 K with the available DFT results of Refs.[30–32], which gives a good match, as shown in **Fig. 5**. The strain-stress curve for $Ti_3C_2T_2$ (T = F and H) are also illustrated in **Fig. 5b** of Ref.[30], which shows that MXene with the oxygen functional group possesses the highest in-plane stiffness. Then, the stress-strain curves for MXenes at other temperatures are calculated and the values of in-plane stiffness, *C*, are extracted from at the corresponding curves, as shown in **Fig. 6**.

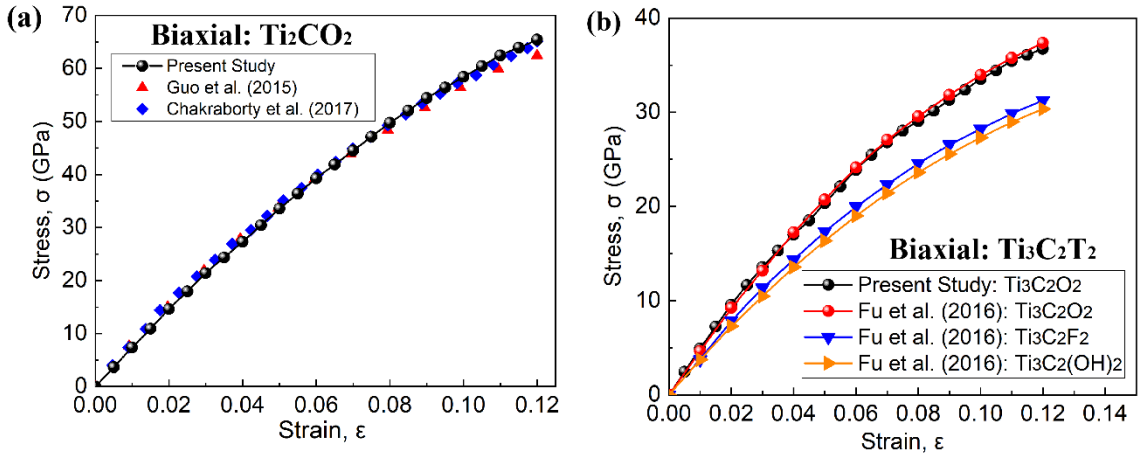

Figure 5. Strain-stress curve of (a) Ti_2CO_2 and (b) $Ti_3C_2T_2$ (T=O, OH, and F) under biaxial tensile strain at 0 K compared with theoretical studies taken from Refs.[30–32].

Temperature-dependent strain-stress curves (**Figs. 6a** and **6b**) show an insignificant difference between the elastic properties at different temperatures. The relatively larger difference

between the stress-strain curves of $Ti_2C_2O_2$ at different temperatures compared with that of $Ti_3C_2O_2$ (**Fig. 6c**) can be attributed to larger lattice expansion Ti_2CO_2 than $Ti_3C_2O_2$ at higher temperatures (**Fig. 2a**). Larger thermal expansion of Ti_2CO_2 compare to $Ti_3C_2O_2$ leads to the weakening of bond strength between atoms to a higher degree (**Fig. 3**).

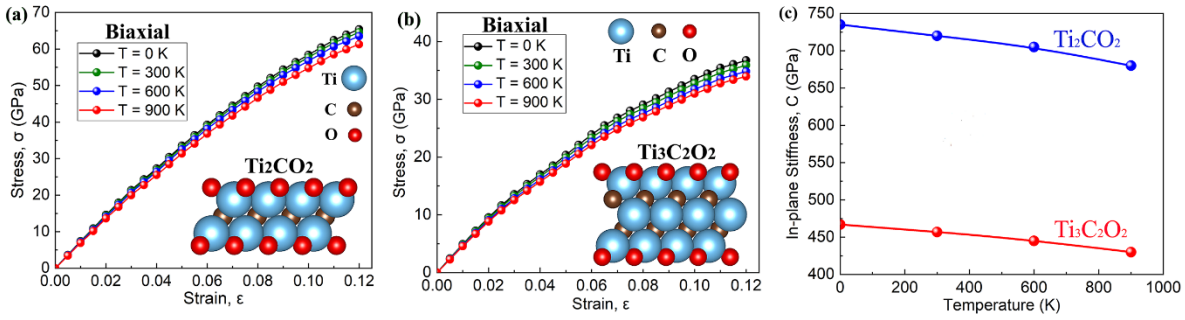

Figure 6. Strain-stress curve of (a) Ti_2CO_2 and (b) $Ti_3C_2O_2$ under biaxial tensile strain at 0 K, 300 K, 600 K, and 900 K. (c) Temperature-dependent in-plane stiffness constant of Ti_2CO_2 and $Ti_3C_2O_2$.

The in-plane stiffness for Ti_2CO_2 is calculated 735 GPa at 0 K, which agrees well with the previous DFT calculation results with the value of 745 GPa[32]. We also calculated in-plane stiffness of 467 GPa for $Ti_3C_2O_2$ at 0 K. By increasing the temperature, the calculated in-plane stiffnesses of MXenes are decreased (**Fig. 6c**), and for Ti_2CO_2 ($Ti_3C_2O_2$), the values decrease to 720 (457) GPa, 705 (445) GPa, and 680 (430) GPa at 300 K, 600 K, and 900 K, respectively. This softening trend is affected by weaker interactions between the atoms due to stronger vibrations at higher temperatures.

Both phonon and elastic stabilities play an important role in the lattice stability conditions of the material. By investigating both stability conditions, we can understand whether the failure of the material is because of the loss of the elastic stability or phonon instability before applying the maximum stress. Many 2D materials are reported to experience phonon softening such as graphene[67–69], BN[69], MoS_2[69,70]. Therefore, we calculated the phonon dispersions for Ti_2CO_2 and $Ti_3C_2O_2$ at state-free state, the biaxial tensile, and compressive strain of 1%, 3%, and 5% in the basal plane. The soft phonon modes are often observed in the calculated phonon dispersions of 2D materials and can affect the calculation of many properties such as thermal

and electrical conductivities of the materials[71]. We found there are no imaginary modes for Ti_2CO_2 and $Ti_3C_2O_2$ at state-free state (see **Figs. S1** and **S2** in Supplementary information). As shown in **Figs. S1 and S2**, the soft phonon modes occur around the Γ point for the tensile as well as compressive strain states (larger than 3%), indicating the softening of the long-wave phonon modes (*i.e.*, elastic instability) and might limit the intrinsic strength for the monolayers. These small branches of the imaginary modes might be associated with the finite size of the supercell applied in this study and the loss of the rotational symmetry because of applying periodic boundary conditions. The phonon spectra of considered MXene systems fulfill the strictest condition for dynamical stability without imaginary modes at a state-free state. Even for the tensile as well as compressive strain states (less than 3%), there is no imaginary modes. The results show that applying a strain larger than 3% leads to making imaginary modes (**Figs. S1 and S2**). Since a strain of 3% is the upper limit strain without imaginary pockets, we considered the strains within 3% for the elastic constant calculations, compatible with recent works on analogous systems[30,31]. In addition, a finite temperature of the experimental condition might further modify the dynamical stability of the monolayer since our phonon calculations are at 0 K[39,40]. Therefore, these structures could be even more stable under experimental conditions. Overall, our results indicate that the imaginary mode enhancement is stronger for $Ti_3C_2O_2$ than Ti_2CO_2. The phonon DOS for these monolayers at the state-free state is shown in **Fig. S3**.

In this study, the stress-strain curves for small biaxial tensile loadings are only used for the elastic constant calculations. Since the results of DFT-QHA is not reliable in the presence of imaginary modes[40], we did not deform the crystal largely to calculate the critical strain at different temperatures.

Since the hexagonal structure of these MXenes is dynamically unstable due to the existence of imaginary modes under the applied strains larger than 3%, we did not study the deformation

mechanism. However, the deformation mechanism of the rectangular structure of Ti_2CO_2 and $Ti_3C_2O_2$ MXenes was previously evaluated using DFT at 0 K[30,31]. For example, it was shown that 2D Ti_2CO_2 can sustain large strains of 20%, 28% and 26.5% under biaxial and uniaxial tensions along with the X and Y directions, respectively.

The Debye temperature of a material is an important thermal quantity that can be used to predict thermodynamic properties such as thermal conductivity. The Debye temperature can be obtained by studying the phonon spectrum of a material. There are three acoustic phonon branches (see **Figs. S1** and **S2**) in the phonon spectra of these monolayers, which are the in-plane longitudinal acoustic modes (LA), transverse acoustic modes (TA), and the out-of-plane transverse acoustic mode (ZA). The ZA mode has a quadratic relation to the wave vector and the TA and LA modes have linear dispersions close to the Γ point and the group velocities of sound can be determined by the slopes of these linear dispersions. The sound speed of the monolayers decreases if the phonon frequency becomes lower. The sound speed of the TA and LA phonons are calculated (ν_{LA} and ν_{TA}), and the data are shown in **Table 3**. The average acoustic Debye temperature for the monolayers can be approximately obtained using the following expression[72]:

$$\frac{1}{\theta_D^3} = \frac{1}{2}\left(\frac{1}{\theta_{LA}^3} + \frac{1}{\theta_{TA}^3}\right) \qquad (8)$$

Where θ_i (i = LA, TA) is determined as $\theta_i = \frac{h\omega_{i,max}}{k_B}$, which is substituted into equation (8) to obtain θ_D as:

$$\theta_D = \frac{h\omega_{LA,max}\omega_{TA,max}}{k_B}\left(\frac{2}{\omega_{LA,max}^3+\omega_{TA,max}^3}\right)^{1/3} \qquad (9)$$

where h and k_B are Planck and Boltzmann constant, respectively, $\omega_{LA,max}$ and $\omega_{TA,max}$ represent the phonon frequency at the zone boundary of the *LA and TA* acoustic modes. The Debye temperature of the monolayers is listed in **Table 3**.

Table 3: Phonon frequency (THz) at the zone boundary and the sound speed (Km s^{-1}) of the *LA and TA* acoustic modes, and Debye temperature θ_D (K) of $Ti_{n+1}C_nO_2$ (n = 1, 2) MXenes.

	$\omega_{LA,max}$	$\omega_{TA,max}$	ν_{LA}	ν_{TA}	θ_D (K)
Ti_2CO_2	9.45	5.15	9.37	6.14	296.22
$Ti_3C_2O_2$	7.91	5.89	9.51	7.64	317.39

The calculated Debye temperature of the Ti_2CO_2 and $Ti_3C_2O_2$ monolayers are 296.22 K and 317.39 K, respectively, which are higher than the calculated Debye temperature of MoS_2 (262.3 K)[72]. The results show that the sound speed of the monolayers decreases with the decrease of Debye temperature, which may lead to lower thermal conductivity. Unfortunately, the Debye temperature of the Ti_2CO_2 and $Ti_3C_2O_2$ were not calculated before and there is no available data for this parameter to compare. However, the Debye temperature of Ti_2AlC MAX-phase was calculated as 719.7 K[73], which is higher than that of the attendant MXene. Since the higher θ_D implies a higher associated thermal conductivity, the results indicate that the thermal conductivity of MAX phases are higher than the attendant MXenes and the thermal conductivity of Ti_2CO_2 (296.22 K) is lower than that of $Ti_3C_2O_2$ (317.39 K).

We also evaluated the temperature-dependent electronic properties of MXenes. Our calculation results at 0 K showed consistency with the previous theoretical investigations[9,20] so that Ti_2CO_2 exhibits semiconducting behavior with the energy gap of 0.24 eV while $Ti_3C_2O_2$ is metallic. However, the results showed that the electronic properties of the MXenes could not significantly change due to the thermal expansion of the monolayers so that 2D Ti_2CO_2 and $Ti_3C_2O_2$ remain semiconductor and metal, respectively, within the temperature range of 1000 K.

III. CONCLUSIONS

In conclusion, we report temperature-dependent mechanical properties of $Ti_{n+1}C_nO_2$ (n = 1, 2) MXenes. Our theoretical calculations predict that Ti_2CO_2 is stiffer than $Ti_3C_2O_2$; however, Ti_2CO_2 softens more than $Ti_3C_2O_2$ with increasing temperature up to 1000 K. It is mainly originated from the larger expansion of the interatomic distances within Ti_2CO_2 compare to

those of $Ti_3C_2O_2$. The bond strength calculations indicate that the chemical bonding between titanium and carbon atoms is stronger in thicker $Ti_3C_2O_2$ than thinner Ti_2CO_2, while oxygen atoms bonds are stronger to outer titanium atoms in Ti_2CO_2 than in $Ti_3C_2O_2$. Our analyses show that the bonds between various atoms in Ti_2CO_2 lose their stiffness more than $Ti_3C_2O_2$ at higher temperatures. This paves the way for an accurate design of MXenes for their high-temperature applications such as structural composite applications and EMI shielding coatings in aerospace.

ACKNOWLEDGMENTS

The authors would like to acknowledge and greatly appreciate the financial support from VISTA which is a basic research program in collaboration between the Norwegian Academy of Science and Letters, and Statoil. The authors would also like to thank the Department of Mechanical and Industrial Engineering at the Norwegian University of Science and Technology (NTNU). The authors also acknowledge generous grants of high-performance computer time from both Vilje and UNINETT Sigma.

REFERENCES

[1] K.S. Novoselov, A.K. Geim1, S. V. Morozov, D. Jiang, Y. Zhang, S. V. Dubonos, I. V. Grigorieva, and A.A. Firsov, Science (80-.). **306**, 666 (2004).

[2] J.N. Coleman, M. Lotya, A.O. Neill, S.D. Bergin, P.J. King, U. Khan, K. Young, A. Gaucher, S. De, R.J. Smith, I. V Shvets, S.K. Arora, G. Stanton, H. Kim, K. Lee, G.T. Kim, G.S. Duesberg, T. Hallam, J.J. Boland, J.J. Wang, J.F. Donegan, J.C. Grunlan, G. Moriarty, A. Shmeliov, R.J. Nicholls, J.M. Perkins, E.M. Grieveson, K. Theuwissen, D.W. Mccomb, P.D. Nellist, and V. Nicolosi, Science (80-.). **331**, 568 (2011).

[3] D. Paciĺ, J.C. Meyer, Ç. Girit, and A. Zettl, Appl. Phys. Lett. **92**, 212 (2008).

[4] L. Li, Y. Yu, G.J. Ye, Q. Ge, X. Ou, H. Wu, D. Feng, X.H. Chen, and Y. Zhang, Nat. Nanotechnol. **9**, 372 (2014).

[5] M. Naguib, M. Kurtoglu, V. Presser, J. Lu, J. Niu, M. Heon, L. Hultman, Y. Gogotsi, and M.W. Barsoum, Adv. Mater. **23**, 4248 (2011).

[6] M. Naguib, O. Mashtalir, J. Carle, V. Presser, J. Lu, L. Hultman, Y. Gogotsi, and M.W. Barsoum, ACS Nano **6**, 1322 (2012).

[7] B. Anasori, M.R. Lukatskaya, and Y. Gogotsi, Nat. Rev. Mater. **2**, 16098 (2017).

[8] Y. Gogotsi and B. Anasori, ACS Nano **13**, 8491 (2019).

[9] M. Khazaei, A. Ranjbar, M. Arai, T. Sasaki, and S. Yunoki, J. Mater. Chem. C **5**, 2488 (2017).

[10] M. Khazaei, A. Mishra, N.S. Venkataramanan, A.K. Singh, and S. Yunoki, Curr. Opin. Solid State Mater. Sci. **23**, 164 (2019).

[11] F. Shahzad, M. Alhabeb, C.B. Hatter, B. Anasori, S.M. Hong, C.M. Koo, and Y. Gogotsi, Science (80-.). **353**, 1137 (2016).

[12] A. Sarycheva, A. Polemi, Y. Liu, K. Dandekar, B. Anasori, and Y. Gogotsi, Sci. Adv. **4**, eaau0920 (2018).

[13] C.E. Ren, M. Alhabeb, B.W. Byles, M. Zhao, B. Anasori, E. Pomerantseva, K.A. Mahmoud, and Y. Gogotsi, ACS Appl. Nano Mater. **1**, 3644 (2018).

[14] M. Zhao, M. Torelli, C.E. Ren, M. Ghidiu, Z. Ling, B. Anasori, M.W. Barsoum, and Y. Gogotsi, Nano Energy **30**, 603 (2016).

[15] M. Naguib, J. Halim, J. Lu, K.M. Cook, L. Hultman, Y. Gogotsi, and M.W. Barsoum, J. Am. Chem. Soc. **135**, 15966 (2013).

[16] Q. Peng, J. Guo, Q. Zhang, J. Xiang, B. Liu, A. Zhou, R. Liu, and Y. Tian, J. Am. Chem. Soc. **136**, 4113 (2014).

[17] G. Fan, X. Li, Y. Ma, Y. Zhang, J. Wu, B. Xu, T. Sun, D. Gao, and J. Bi, New J. Chem. **41**, 2793 (2017).

[18] B. Anasori, C. Shi, E.J. Moon, Y. Xie, C.A. Voigt, P.R. Kent, S.J. May, S.J. Billinge, M.W. Barsoum, and Y. Gogotsi, Nanoscale Horizons **1**, 227 (2016).

[19] J.L. Hart, K. Hantanasirisakul, A.C. Lang, B. Anasori, D. Pinto, Y. Pivak, J.T. Van Omme, S.J. May, Y. Gogotsi, and M.L. Taheri, Nat. Commun. **10**, 522 (2019).

[20] M. Khazaei, M. Estili, N.S. Venkataramanan, T. Sasaki, Y. Sakka, C. Chung, M. Arai, and Y. Kawazoe, Adv. Funct. Mater. **23**, 2185 (2013).

[21] H. Lashgari, M.R. Abolhassani, A. Boochani, S.M. Elahi, and J. Khodadadi, Solid State Commun. **195**, 61 (2014).

[22] H. Kim, B. Anasori, Y. Gogotsi, and H.N. Alshareef, Chem. Mater. **29**, 6472 (2017).

[23] M. Khazaei, M. Arai, T. Sasaki, M. Estili, and Y. Sakka, Phys. Chem. Chem. Phys. **16**, 7841 (2014).

[24] S. Cho, B. Anasori, C. Kim, Y. Choi, J. Kim, and Y. Gogotsi, ACS Nano **12**, 986 (2018).

[25] X.F. Yu, Y.C. Li, J.B. Cheng, Z.B. Liu, Q.Z. Li, W.Z. Li, X. Yang, and B. Xiao, ACS Appl. Mater. Interfaces **7**, 13707 (2015).

[26] Z.W. Seh, K.D. Fredrickson, B. Anasori, J. Kibsgaard, A.L. Strickler, M.R. Lukatskaya, Y. Gogotsi, T.F. Jaramillo, and A. Vojvodic, ACS Energy Lett. **1**, 589 (2016).

[27] L.Y. Gan, D. Huang, and U. Schwingenschlögl, J. Mater. Chem. A **1**, 13672 (2013).

[28] G. Plummer, B. Anasori, Y. Gogotsi, and G.J. Tucker, Comput. Mater. Sci. **157**, 168 (2019).

[29] A. Lipatov, H. Lu, M. Alhabeb, B. Anasori, A. Gruverman, Y. Gogotsi, and A. Sinitskii, Sci. Adv. **4**, eaat0491 (2018).

[30] Z.H. Fu, Q.F. Zhang, D. Legut, C. Si, T.C. Germann, T. Lookman, S.Y. Du, J.S. Francisco, and R.F. Zhang, Phys. Rev. B **94**, 1 (2016).

[31] Z. Guo, J. Zhou, C. Si, and Z. Sun, Phys. Chem. Chem. Phys. **17**, 15348 (2015).

[32] P. Chakraborty, T. Das, D. Nafday, L. Boeri, and T. Saha-Dasgupta, Phys. Rev. B **95**, 184106 (2017).

[33] M. Kurtoglu, M. Naguib, Y. Gogotsi, and M.W. Barsoum, MRS Commun. **2**, 133 (2012).

[34] S. Wang, J.X. Li, Y.L. Du, and C. Cui, Comput. Mater. Sci. **83**, 290 (2014).

[35] X.H. Zha, K. Luo, Q. Li, Q. Huang, J. He, X. Wen, and S. Du, Eur. Lett. **111**, 26007 (2015).

[36] C. Lee, X. Wei, J.W. Kysar, and J. Hone, Science (80-.). **321**, 385 (2008).

[37] M. Yi and Z. Shen, J. Mater. Chem. A **3**, 11700 (2015).

[38] J.W. Suk, R.D. Piner, J. An, and R.S. Ruoff, ACS Nano **4**, 6557 (2010).

[39] A. Togo, F. Oba, and I. Tanaka, Phys. Rev. B **78**, 134106 (2008).

[40] A. Togo and I. Tanaka, Scr. Mater. **108**, 1 (2015).

[41] J. Guo, B. Legum, B. Anasori, K. Wang, P. Lelyukh, Y. Gogotsi, and C.A. Randall, Adv. Mater. **30**, 1801846 (2018).

[42] A. Togo, L. Chaput, I. Tanaka, and G. Hug, Phys. Rev. B **81**, 174301 (2010).

[43] G. Kresse and J. Furthmiiller, Comput. Mater. Sci. **6**, 15 (1996).

[44] G. Kresse and J. Furthmüller, Phys. Rev. B - Condens. Matter Mater. Phys. **54**, 11169 (1996).

[45] G. Kresse and J. Hafner, Phys. Rev. B **49**, 14251 (1994).

[46] G. Kresse and J. Hafner, Phys. Rev. B **47**, 558 (1993).

[47] J.P. Perdew and A. Zunger, Phys. Rev. B **23**, 5048 (1981).

[48] J.P. Perdew, M. Ernzerhof, and K. Burke, Phys. Rev. Lett. **77**, 3865 (1996).

[49] H.J. Monkhorst and J.D. Pack, Phys. Rev. B Solid State 5188 (1976).

[50] P.G.S.B.S. de G. Andrea Dal Corso, J. Chem. Phys. **134**, (2011).

[51] X. Gonze and C. Lee, Phys. Rev. B - Condens. Matter Mater. Phys. **55**, 10355 (1997).

[52] S. Grimme, J. Comput. Chem. **27**, 1787 (2006).

[53] R. Khaledialidusti, A.K. Mishra, and A. Barnoush, AIP Adv. **9**, 065021 (2019).

[54] T. Shao, B. Wen, R. Melnik, S. Yao, Y. Kawazoe, and Y. Tian, J. Appl. Phys. **111**, 083525 (2012).

[55] T. Shao, B. Wen, R. Melnik, S. Yao, Y. Kawazoe, and Y. Tian, J. Chem. Phys. **137**, (2012).

[56] M. Topsakal, S. Cahangirov, and S. Ciraci, Appl. Phys. Lett. **96**, (2010).

[57] N. Zhang, Y. Hong, S. Yazdanparast, and M.A. Zaeem, 2D Mater. **5**, (2018).

[58] D. Yoon, Y. Son, and H. Cheong, Nano Lett. **11**, 3227 (2011).

[59] M. Magnuson, J. Halim, and L.-åke Näslund, J. Electron Spectros. Relat. Phenomena **224**, 27 (2018).

[60] M. Seredych, C.E. Shuck, D. Pinto, M. Alhabeb, E. Precetti, G. Deysher, B. Anasori, N. Kurra, and Y. Gogotsi, Chem. Mater. **31**, 3324 (2019).

[61] R. Dronskowski, M. Festkbrperforschung, and P.E. Blochl, J. Phys. Chem. 8617 (1993).

[62] M. Küpers, P.M. Konze, S. Maintz, S. Steinberg, A.M. Mio, O. Cojocaru-MirØdin, M. Zhu, M. Müller, M. Luysberg, J. Mayer, M. Wuttig, and R. Dronskowski, Angew. Chemie, Int. Ed. **56**, 10204 (2017).

[63] M. Khazaei, A. Ranjbar, K. Esfarjani, and D. Bogdanovski, Phys. Chem. Chem. Phys. **20**, 5879 (2018).

[64] M. Khazaei, J. Wang, M. Estili, A. Ranjbar, S. Suehara, M. Arai, K. Esfarjani, and S.

Yunoki, Nanoscale **11**, 11305 (2019).

[65] Q. Yang, W. Lengauer, T. Koch, M. Scheerer, and I. Smid, J. Alloys Compd. **309**, 5 (2000).

[66] V.I. Ivashchenko, P.E.A. Turchi, A. Gonis, L.A. Ivashchenko, and P.L. Skrynskii, Metall. Mater. Trans. A Phys. Metall. Mater. Sci. **37**, 3391 (2006).

[67] C.A. Marianetti and H.G. Yevick, Phys. Rev. Lett. **245502**, 1 (2010).

[68] C. Si, W. Duan, Z. Liu, and F. Liu, Phys. Rev. Lett. **226802**, 1 (2012).

[69] E.B. Isaacs and C.A. Marianetti, Phys. Rev. B **184111**, 2 (2014).

[70] T. Li, Phys. Rev. B **235407**, 1 (2012).

[71] J. Carrete, W. Li, L. Lindsay, D.A. Broido, and L.J. Gallego, Mater. Res. Lett. **4**, 204 (2016).

[72] B. Peng, H. Zhang, H. Shao, Y. Xu, X. Zhanga, and H. Zhua, **6**, 5767 (2016).

[73] M. Khazaei, M. Arai, T. Sasaki, and M. Estili, J. Phys. Condens. Matter **26**, 505503 (2014).

Supporting Information

Temperature-dependent mechanical properties of 2D $Ti_{n+1}C_nO_2$ (n = 1, 2) MXene monolayers

Rasoul Khaledialidusti,[*1] Babak Anasori,[*2] Afrooz Barnoush[1]

[1]Department of Mechanical and Industrial Engineering, Norwegian University of Science and Technology (NTNU), 7491 Trondheim, Norway.
[2] Department of Mechanical and Energy Engineering, and Integrated Nanosystems Development Institute, Purdue School of Engineering and Technology, Indiana University – Purdue University Indianapolis, Indianapolis, IN 46202, USA.

Dynamical stability

The phonon spectra of 2D $Ti_{n+1}C_nO_2$ (n = 1, 2) at state-free state and biaxial tensile and compressive strain of 1%, 3%, and 5% in the basal plane are shown in **Figs. S1** and **S2**, which passes several high symmetry directions ($\Gamma_{(0,0,0)} \rightarrow M_{(1/2,0,0)} \rightarrow K_{(1/3,1/3,0)} \rightarrow \Gamma_{(0,0,0)}$).

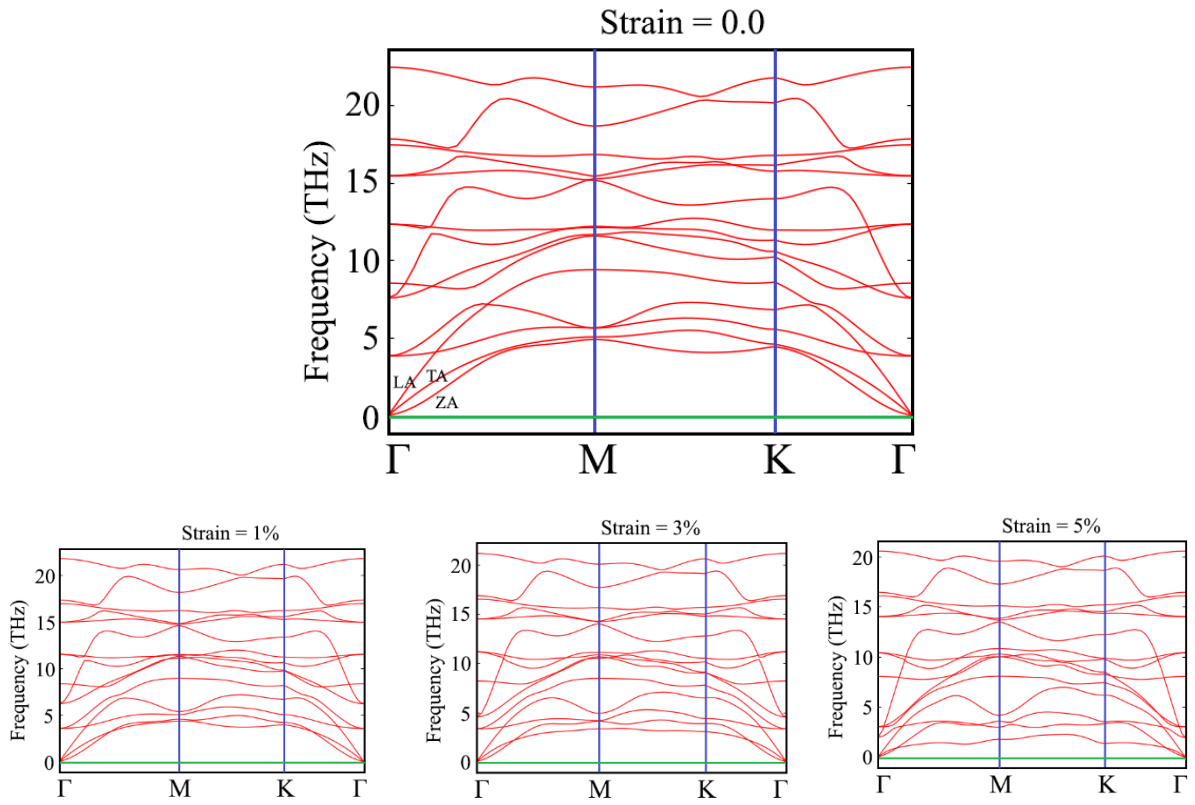

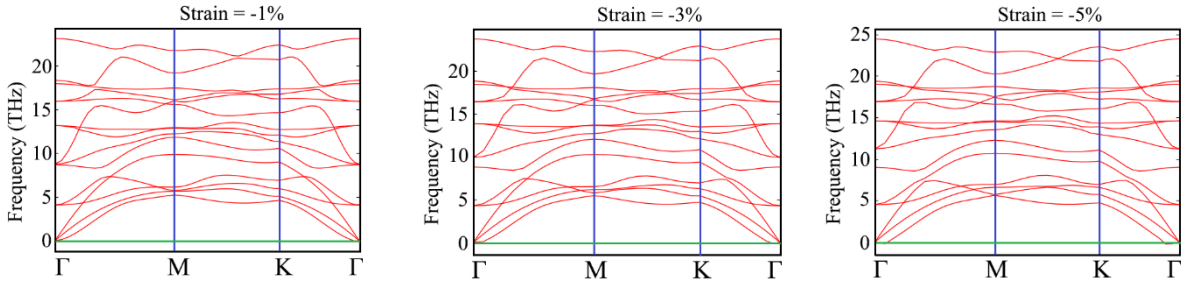

Figure S1. Phonon dispersion curves for Ti_2CO_2 at state-free state and biaxial tensile and compressive strain of 1%, 3%, and 5% in the basal plane.

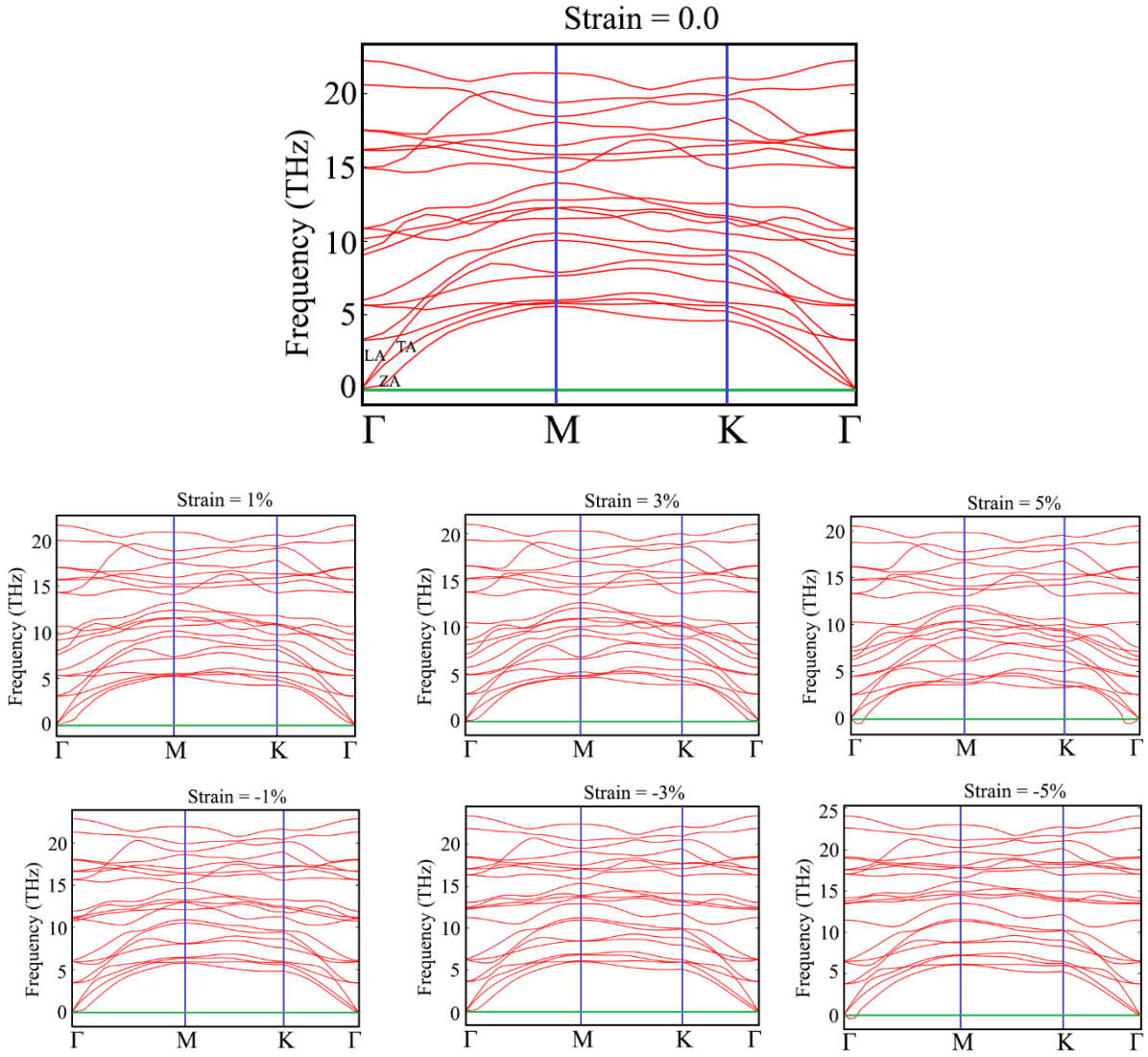

Figure S2. Phonon dispersion curves for $Ti_3C_2O_2$ at the state-free state and biaxial tensile and compressive strain of 1%, 3%, and 5% in the basal plane.

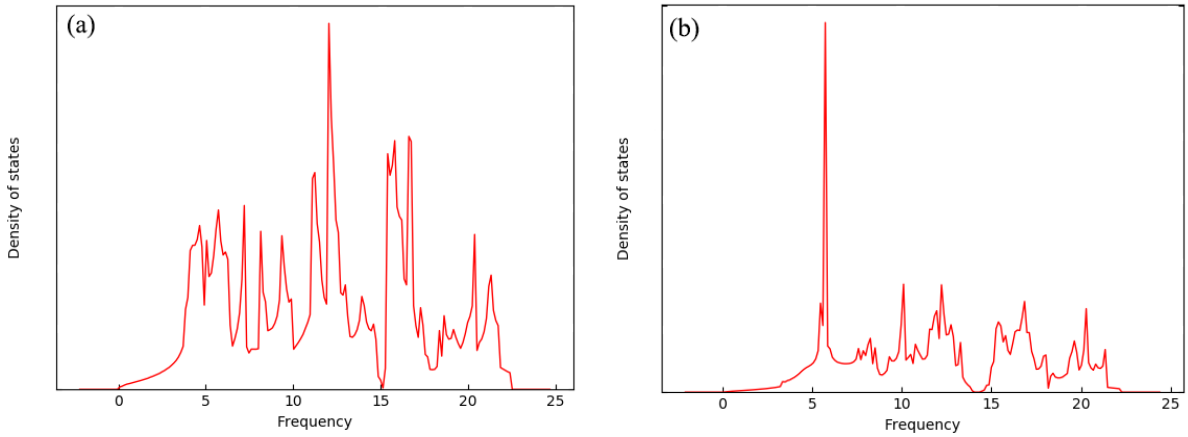

Figure S3. Calculated phonon DOS of (a) Ti_2CO_2 and (b) $Ti_3C_2O_2$ monolayers at the state-free state.